

**Morphology and kinematics of Planetary Nebulae. I. A  
new modeling tool.**

C. Morisset<sup>1,2</sup>, R. Gruenwald<sup>2</sup>,  
and  
S. M. Viegas<sup>2</sup>

Received \_\_\_\_\_; accepted  
\_\_\_\_\_

arXiv:astro-ph/9912157v1 8 Dec 1999

---

<sup>1</sup>Laboratoire d'Astronomie Spatiale, Traverse du Siphon, Les Trois Lucs,  
13012 Marseille, France <morisset@astrsp-mrs.fr>

<sup>2</sup>Instituto Astronômico e Geofísico, USP, Avenida Miguel Stefano, 4200  
CEP 04301-904 São Paulo, SP, Brazil <ruth@agn1.iagusp.usp.br> and  
<viegas@agn1.iagusp.usp.br>

## ABSTRACT

We present a new modeling tool for planetary nebulae, based on 3D photoionization calculations. Our goal is to show that all the information provided by observations, regarding kinematics and morphology, have to be consistently accounted for, in order to get a real insight of the object. Only 3D simulations offer this possibility. From models for two theoretical PNe, we show that the enhancement in the equatorial zone observed in several PNe is not necessarily due to a density gradient, as usually interpreted. It is also shown that asymmetric velocity profiles often observed (e.g., Gesicki et al. 1998) can be easily reproduced. Observations providing a better insight on the morphology of the PN are discussed.

### 1. Introduction

Planetary Nebulae (PNe) show different morphologies, but since the works of Kwok et al. (1978) and Balick (1987), it is possible to reproduce their observed shape basically with two types of geometry: spherico-elliptical ones and bi-polar ones (also called butterfly), all of them axisymmetrical in a first approximation.

Observed morphological differences may result from (1) different orientation of the line-of-sight and of the axis of symmetry and (2) the age of the nebula. Morphological sequences have been studied by Balick (1987), Pascoli (1990) and Zhang & Kwok (1998), among others. Evolutionary theories based on the generalized interacting stellar wind model (GISW, see Franck & Mellema 1994 and references therein) seem to confirm these interpretations.

Information obtained from photometric imaging and intermediate resolution spectra have been complemented by narrow band images (e.g., Sahai et al. 1997) and high resolution spectra (e.g., Walton et al. 1990), providing information on the kinematics of the nebula.

The various observations can not be correctly interpreted without detailed modeling, which must consistently reproduce all observational data. For some years, most of the data have been analysed by GISW models (Soker & Livio 1989; Mellema, Eulderink & Icke 1991; Icke, Balick & Frank 1992), which account only for the gas dynamics. A more realistic model to analyse morphologies and kinematics of PNe was proposed by Frank & Mellema (1994). These 2D simulations include radiation processes and ionization balance,

while the gas cooling through line emission is obtained from polynomial approximations for the line emissivities (Balick et al. 1993).

Here a new modeling tool for studying the morphology and kinematics of PNe is presented. Assuming a velocity field, the results of a 3D photoionization code (Gruenwald, Viegas & Broguière 1997, hereinafter GVB) are used to generate images to be directly confronted with various kinds of observations. We address general PNe issues, raised by the observations, as gas distribution and morphology, brightness enhancement at the equatorial ring, the asymmetric emission line profiles (e.g. Gesicki et al. 1998).

The computational methods used to model planetary nebulae are presented in §2. Results for two theoretical objects are shown and discussed in §3. The conclusions appear in §4.

## 2. Computational methods

### 2.1. The 3D photoionization code

The 3D photoionization code is described in GVB. The input parameters are the ionizing radiation spectrum, the gas chemical composition and the spatial density distribution. The nebula is divided in a great number of cells. Inside each cell the physical conditions, which are obtained from the ionization equilibrium and thermal balance, are assumed homogeneous. For each cell, the output are the emissivity of atomic lines and the physical conditions of the gas (electronic density, fractional abundances, electronic temperature). The number of cells defines the numerical accuracy. It depends on the specific object under analysis, as well as on the computer memory.

The effect of the diffuse radiation can be accounted for. However, in its present version, the required computational time is too high (few tens of the on-the-spot case). Thus, we assume here the on-the-spot approximation, using case B parameters of Péquignot et al. (1991) for the hydrogen recombination coefficient. The effect is small enough and do not affect the general conclusions presented here. The  $H\beta$  luminosity is underestimated by 30% or less when the on-the-spot approximation is assumed. The percentage depends on the stellar temperature: the higher the stellar temperature the bigger the underestimation of the  $H\beta$  luminosity. The differences between the line intensities relative to  $H\beta$  is less than 20%, except for the weak lines ( $< 0.05 H\beta$ ).

Emission line images are obtained after a line-of-sight integration. The calculations are made assuming a stationary

approximation. In order to analyse the kinematics, a velocity field is assumed after obtaining the photoionization results for each cell. The data cubes, containing the results generated by the 3D code for the cells, are read by an IDL (RSI) code which provides the tools for filtering, rotation, projection, statistics, velocity maps and echellograms, as described below.

In this paper, only axi-symmetric nebulae will be studied. In order to increase the number of cells used in the calculations (increasing the numerical accuracy), 1/8 of the nebula is modeled. For the calculated 1/8 of the nebula, the number of cells is  $50^3 = 125\,000$ . In this case, the ionizing source is placed at one of the corners of the large cube. In order to restore the whole nebula, with the ionizing source at the center, the remaining 7/8 are added up, using the calculated 1/8 after appropriate rotations.

## 2.2. Rotations

The nebula is defined in a XYZ coordinate system, where X is the axis of symmetry, the origin being at the ionizing source (center of the rebuilt cube). The rotations and projections operate on a data cube of  $xyz$  coordinates. In the following, the line of sight used for the projections will be  $y$ . Before any rotation the origins, as well as the axes of the XYZ and  $xyz$  coordinate systems, are coincident.

The rotations of the data cubes are performed in the  $xyz$  space, plane by plane, using the two-dimensional ROT function of IDL, in a  $\sqrt{3}$  times greater cube to avoid losing information. If needed, up to three rotations around the three axes of the cube can be performed, in any order.

If rotations around more than one axis are necessary, it is easier if one starts with a rotation around an axis perpendicular to both the axis of symmetry of the nebula ( $X$ ) and the axis along the line-of-sight ( $y$ ). In order to compare the theoretical images to observations, a second rotation of the data cube may be needed.

## 2.3. Emission line images

For each emission line the 3D code provides the luminosity in each cell. The total luminosity (corresponding to the whole nebula), as well as the intensity corresponding to a given aperture, can be obtained and compared to observational data.

The projected image on the plane of the sky is obtained for a given emission line by integrating the emissivities of the cells lying along the line-of-sight which is taken perpendicular to one of the cube faces.

Maps of emission line intensity ratios can also be obtained, especially those used to obtain the PN physical conditions. These maps can be transformed into density or temperature maps using relationships (e.g., Alexander & Balick 1997) between the projected line intensity ratios and these quantities.

## 2.4. Line profiles

In order to obtain a line profile, a cube of velocities at the same resolution as the 3D code output is generated according to a predefined law. In this paper we assume a radial velocity field. Since the projection is made on the  $y$ -axis direction, only the corresponding component of the velocity is retained ( $V_y(x, y, z)$ ). For each emission line, a velocity profile is generated, for each line-of-sight, by

$$\phi_\lambda(v, x, z) = \sum_y \frac{\epsilon_\lambda(x, y, z)}{\sqrt{\pi} \cdot \xi(x, y, z)} \cdot e^{-\left[\frac{\Delta V(v, x, y, z)}{\xi(x, y, z)}\right]^2}$$

with:

$$\Delta V(v, x, y, z) = V_y(x, y, z) - v$$

$$\xi(x, y, z) = \sqrt{V_{th}^2(x, y, z) + V_T^2}$$

$$V_{th}(x, y, z) = \sqrt{2kT_e(x, y, z)/Am_H}$$

where  $\epsilon_\lambda(x, y, z)$  is the emissivity of a given line inside the  $xyz$  cell,  $V_T$  is the turbulent velocity and  $V_{th}(x, y, z)$  is the thermal velocity of the corresponding atom of mass number  $A$ . The local electronic temperature  $T_e(x, y, z)$  is consistently obtained from the 3D code.

Velocity contour maps and P-V maps (echellograms) can be generated. After masking through an aperture and convoluting with an instrumental profile, the theoretical data can be compared to observations.

## 2.5. Average physical quantities

For each emission line, average physical quantities of the region where the line is produced can be obtained. Average values for the electron temperature, density, hydrogen ionization, and velocity are calculated by weighting these quantities by the line emissivity. The general assumed formula is:

$$\langle Q \rangle_\lambda = \frac{\sum Q(x, y, z) \cdot \epsilon_\lambda(x, y, z)}{\sum \epsilon_\lambda(x, y, z)}$$

where  $Q$  is replaced by  $T_e$ ,  $n_e$ ,  $H^+/H$  or  $v$ . These quantities can be obtained for the whole nebula, as well as for lines-of-sight characterized by an  $xz$  position, summing on  $xyz$  or  $y$ , respectively. Notice that Peimbert (1967) defined some

of these quantities weighting by  $n_e.n(X^i)$  instead of by the line emissivity.

Dimensionless temperature fluctuations ( $t^2$ ) and density fluctuations ( $n_e^2$ ) can also be computed:

$$Q_\lambda^2 = \frac{\sum(Q(x, y, z) - \langle Q \rangle_\lambda)^2 \cdot \epsilon_\lambda(x, y, z)}{\langle Q \rangle_\lambda^2 \sum \epsilon_\lambda(x, y, z)}$$

Empirical methods for chemical abundance determination are usually based on these averaged quantities and fluctuations, defined for the whole nebula. They have been generally applied to point-to-point observations, assuming a spherical symmetry. In this case, however, the method is not always correct, even for spherically symmetric objects (Gruenwald & Viegas 1992). A real nebulae is not necessarily symmetric and homogeneous. Therefore, only 3D models can provide tools for improving the empirical methods.

### 3. Application to planetary nebulae

#### 3.1. Models

Two simple theoretical PNe will be assumed (A and B) with two possible geometries (1 and 2). Models A correspond to higher black-body temperature, higher density and higher luminosity than models B (Table 1). On the other hand, type 1 models have a spherical cavity surrounded by a shell with a density gradient; the density increases linearly with the angle, from the pole to the equator. Type 2 models have a prolate elliptical cavity surrounded by a constant density shell. These two geometries are two simple cases which can reproduce the bipolar brightness enhancement usually shown by PN images. Surely, the geometry of real objects is determined by hydrodynamics. Thus, a further improvement, out of the scope of this paper, would be to use the 3D photoionization code adopting a geometry obtained from a hydrodynamic code.

The input parameters related to the density distribution are given in Table 1. The following notation is used:  $n_H(\text{cav})$  is the cavity density;  $n_H(\text{shell})$  is the shell density (type 2 models), or its range (type 1);  $R_{\text{inner}}$  is the cavity radius (type 1) or the semi-axis of the elliptical cavity (type 2). Models A are inspired on the canonical PN of the Paris workshop (Péquignot 1986, see also Ferland et al. 1995).

The adopted chemical abundances are the same for the four models, and are taken from the canonical PN, i.e., H:1.0, He:0.1, C:3(-4), N:1(-4), O:6(-4), Ne:1.5(-4), Mg:3(-5), Si:3(-5), S:1.5(-5), Cl:4(-7), Ar:6(-6), Fe:1(-7).

For all models, the PN is radiation bound in all directions.

#### 3.2. Spectroscopical results

Results for the 3D models A1, A2, B1, and B2, corresponding to the whole nebula, are listed in Table 1. Only line intensities of the main emission lines, relative to  $H\beta$ , are given, as some average quantities obtained from line ratios, using Alexander & Balick (1997) fits or the formulae given in §2.5 (lower part of the table).

The differences between the results of A1 and A2 models are not significant. For both models, the results for line intensities are within the values obtained for the canonical PN (spherical symmetry and constant density) with the various 1D photoionizing codes (Ferland et al. 1995). Notice that our results were obtained using the on-the-spot approximation (see §2.1). From the point of view of the emission-line spectra, as well as of the derived physical conditions, no conclusion about the nebula geometry can be drawn, since both geometries lead to similar spectroscopical results. The same is true for a planetary nebulae with a lower stellar temperature, lower luminosity and density, as seen from the similarity between the results of models B1 and B2.

For both (A and B) types of nebula, the determination of temperature and density, from the line ratios or from the formulae (§2.5), are consistent within 10%. The electronic temperatures obtained from the [OIII] and [NII] line ratios are different because these lines come from different regions.

EDITOR: PLACE TABLE 1 HERE.

#### 3.3. Imaging

Emission line images often show a brightness enhancement which is usually interpreted as the signature of a density gradient in the equatorial belt of PNe (Weedman 1968; Khan & West 1985; Aaquist & Kwok 1996; Zhang & Kwok 1998). The images of  $H\beta$ , [O III] $\lambda$ 5007, He II $\lambda$ 4686, and [N II] $\lambda$ 6583 obtained from models A and B are given, respectively, in Figs. 1 and 2. The nebulae are projected along the Y axis (no rotation). The top four panels correspond to type 1 models, while the bottom four ones to type 2 models. Notice that type 1 and 2 models have different geometries, which might reproduce the observed enhancement. In type 1 models, the gas density increases linearly with the angle from the pole to the equator, and is distributed around an inner spherical cavity. On the other hand, in type 2 models the gas is uniformly distributed around a prolate elliptical cavity. As suggested by the figures, the models are able to generate the brightness enhancement. Notice that the line intensity enhancement is due to the higher density in the

equator for type 1 models, whereas, for type 2 models, it appears because the density of the *ionizing photons* reaching the inner edge of the gas is higher in the direction along the minor axis.

However, the real geometry can not be easily inferred from the shape suggested by the images. In fact, model A1 images show an ellipsoidal shape, while for model A2 the shape suggests a spherical distribution, which is the opposite of the adopted shapes for the inner cavities. This contrasting behavior is less pronounced in models B, with lower stellar temperature and luminosity, as well as with lower density, than models A. The image shape given by model A2 is defined by the ionizing radiation dilution, independently of the gas distribution. On the other hand, in model B2 the main factor defining the image shape is the shape of the inner cavity.

From these results, we see that narrow band imaging may not differentiate the nebular geometry as previously assumed. In the next section we discuss a possible geometry indicator.

EDITOR: PLACE FIGURE 1 HERE.

EDITOR: PLACE FIGURE 2 HERE.

### 3.4. Density maps

As shown above, spectroscopic results and emission line imaging do not provide enough constraints on the nebula density distribution. The density indicator generally used is the [SII] line intensity ratio. The density maps obtained from the [S II] ratio (see §2.3) are shown in Fig. 3 for models B1 (top panel) and B2 (bottom panel). As expected, the density gradient adopted for model B1 is clearly perceived.

EDITOR: PLACE FIGURE 3 HERE.

### 3.5. Velocity profiles

High resolution observation of PNe emission lines often show double-peaked profiles, interpreted as the emission of a geometrically thin expanding shell. Usually, the two peaks are not symmetric (see Gesicki et al. 1996, 1998 for seven PNe, and Dudziak et al. 1999 for NGC3132). If the asymmetry were due to local extinction, the blue peak should always be more intense than the red one. Since this is not the case, another explanation for the asymmetry must be found.

In the following, the effect on the line profiles, due to geometry and orientation, will be discussed. We show that the asymmetry in the line profiles can be reproduced using a 3D photoionization code and the numerical tools described above (§2). In order to illustrate these results, one case is presented, using model A1 with a given velocity law. A linear law, as used by Sahu & Desai (1986), is quite natural. In the following we adopted  $\vec{V} = \alpha \times \vec{r}/r_o$ , with  $\alpha = 20$  km/s and  $r_o = 2.4 \times 10^{17}$  cm (maximum of the [O III] emissivity). The velocity profiles obtained after the rotation of the nebula by  $50^\circ$  around the  $z$ -axis and projection along the  $y$  axis are shown in Fig. 4. Each profile corresponds to a synthetic observation at a different position in the nebula. The assumed positions and aperture are shown in the upper panel, over the [O III] image. A turbulent velocity of 2 km/s was taken into account. Such value for the turbulent velocity is small, so that the adopted velocity field dominates the line profile. No convolution through an instrumental profile was applied.

As seen in the figure, the profile changes from one region to another. Depending on the position, asymmetric profiles are obtained, including asymmetric double-peaked profiles. For positions at the right side of the nebula the double peaked profiles, when asymmetric, show the blue peak more intense than the red one. On the other hand, due to the rotation around the  $z$ -axis, a red asymmetry (not shown in the figure) would be obtained for positions on the left side of the image.

The mean velocity (as defined in §2.5) of the [O III] zone is  $\langle V \rangle_{5007} = 22.1$  km/s, which is comparable to what could be found from the peak separation on the profile corresponding to the synthetic observation of the central part of the nebula.

EDITOR: PLACE FIGURE 4 HERE.

Other velocity laws, suggested by hydrodynamic calculations, could be adopted when discussing observations from real objects.

### 3.6. PV diagrams

More accurate than line profiles observed at discrete positions, Position-Velocity (PV) diagrams (also called echellograms) provide an effective diagnostic for the geometry of PNe. In the case of line tilts (Guerrero et al. 1997), PV-diagrams give constraints on the inclination of the PN (Marston et al. 1998). The observations and the 2D model of NGC 650-1 (Bryce et al. 1996) is another example of the use of PV-diagrams to deduce the geometrical properties of

PNe. Such a model is not detailed enough to reproduce the differences between the observed emission of [N II] $\lambda$ 6584 and [O III] $\lambda$ 5007. A 3D photoionization code is needed. PV-diagrams obtained from our model A1 rotated by  $50^\circ$  around the  $z$  axis and projected on the  $y$  direction are shown in Fig. 5. The upper-left panel shows the [O III] $\lambda$ 5007 image of the nebula. The upper-right and lower-left panels show PV-diagrams obtained through vertical and horizontal centered slits, respectively. The lower-right panel illustrates iso-velocity contours, for  $V = 9$  km/s. The  $z$ -PV-diagram shows the signature of the tilt of the PN around the  $z$ -axis, while the absence of an asymmetry in the  $x$ -PV diagram indicates that the  $Z$  axis of the nebula is perpendicular to the line of sight and coincides with the  $z$ -axis. Such simulation is available from the 3D code for all the emission lines and is a very powerful tool to model high resolution observations like the ones from the TAURUS instrument (Walton et al. 1990).

EDITOR: PLACE FIGURE 5 HERE.

#### 4. Concluding remarks

This paper illustrates the importance of 3D photoionization simulations when analyzing the various observational data currently obtained for PNe. Regarding the stellar temperature and luminosity, two different PNe are simulated. For each one, two density distributions are assumed, in order to test the constraints on the nebula geometry provided by the data. For each kind of observation (emission line spectroscopy, emission line imaging, emission line profiles) the results obtained with the two different geometries are compared.

Regarding line emission from the whole nebula, the emission line ratios do not discriminate between the two possible density distributions since the two models have the same average density, giving similar [S II] line intensity ratios. Emission line imaging showing an ellipsoidal shape with an intensity enhancement on the minor axis is obtained with both density distributions. Thus, this kind of observational data do not provide a method to distinguish between the two distributions. Density maps, obtained from emission line ratios that are density indicators, can provide one of the keys to the geometry puzzle, as shown in §3.4. The other key, related to the orientation of the axis of symmetry of the nebula, comes from the emission line profiles observed in different locations of the nebula. An asymmetric double-peaked profile is usually observed in PNe, but until now never theoretically reproduced by photoionization models.

It can be generated assuming that the expansion velocity increases outward and that the axis of symmetry of the nebula makes an angle with the plane of the sky (see §4). The axis of symmetry tilt can also be visualized on the echelograms (§5). Notice that double-peaked profiles are also generated by pure hydrodynamic models (Mellema 1994).

In brief, the different kinds of observations that are now available for planetary nebulae can only provide a complete insight of the object and its properties, if they are confronted with the results of photoionization simulations from a 3D code.

C. Morisset is thankful to IAGUSP for the hospitality during his post-doctoral visit. This work was supported by CNPq (n. 304077/77-1 and n. 150162/96-0), FAPESP (n. 98/01922-7), and PRONEX/FINEP (n. 41.96.0908.00). The calculations were performed with a DEC/ALPHA 3000 workstation (FAPESP n. 93/4348-6).

#### REFERENCES

- Aaquist, O. B. & Kwok, S. 1996, ApJ, 462, 813  
 Alexander, J. & Balick, B. 1997, AJ, 114, 713  
 Balick, B. 1987, AJ, 94, 671  
 Balick, B., Mellema, G. & Frank, A. 1993, A&A, 275, 588  
 Bryce, M., Mellema, G., Clayton, C. A., Meaburn, J., Balick, B. & Lopez, J. A. 1996, A&A, 307, 253  
 Dudziak, G., Walsh, J. R. & Walton, N. A. 1999, A&A, submitted  
 Ferland, G. et al. 1995, in *The Analysis of Emission Lines: A Meeting in Honor of the 70th Birthdays of D. E. Osterbrock & M. J. Seaton*. Eds. R. Williams & M. Livio, Cambridge University Press, p. 83.  
 Franck, A. & Mellema, G. 1994, ApJ, 430, 800  
 Icke, V., Balick, B. & Frank, A. 1992, A&A, 253, 224  
 Gesicki, K., Acker, A. & Szczerba, R. 1996, A&A, 309, 907  
 Gesicki, K., Zijlstra, A. A., Acker, A. & Szczerba, R. 1998, A&A, 329, 265  
 Guerrero, M. A., Manchado, A. & Chu, Y. -H. 1997, ApJ, 487, 328  
 Gruenwald, R., Viegas, S. M. 1992, ApJS 78, 153  
 Gruenwald, R., Viegas, S. M. & Brogière, D. (GVB) 1997, ApJ, 480, 283  
 Khan, F. D. & West, K. A. 1985, MNRAS, 212, 837

- Kwok, S., Purton, C. R. & Fitzgerald, P. M. 1978, *ApJ*, 219, L125
- Marston, A. P., Bryce, M., Lopez, J. A., Palmer, J. W. & Meaburn, J. 1998, *A&A*, 329, 683
- Mellema, G., *A&A*, 290, 915
- Mellema, G., Eulderink, F. & Icke, V. 1991, *A&A*, 252, 718
- Pascoli, G. 1990, *A&A*, 232, 184
- Péquignot, D. 1986, *Publications de l'Observatoire de Paris, Proceedings of a Workshop on Model Nebulae*, held at Observatoire de Meudon, July 8-19, 1985, Paris: Observatoire de Paris-Meudon, 1986, edited by Péquignot, D.
- Péquignot, D., Petitjean, P. & Boisson, C. 1991, *A&A*, 251, 680
- Peimbert, M. 1967, *ApJ*, 150, 825
- Sahai, R., Trauger, J., Bujarrabal, V., & Wfpc2 Id Team 1997, *American Astronomical Society Meeting*, 191, 1508
- Sahu, K. C. & Desai, J. N. 1986, *A&A*, 161, 357
- Saurer, W. 1997, *A&A*, 328, 641
- Shaw, R. A. & Dufour, R. J. 1995, *PASP*, 107, 8965
- Soker, N. & Livio, M. 1989, *ApJ*, 339, 268
- Walton, N. A., Walsh, J. R. & Sahu, K. C. 1990, *A&A* 230, 445
- Weedman, D. W. 1968, *ApJ*, 153, 49
- Zhang, C. Y. & Kwok, S. 1998, *ApJS*, 117, 341
- Fig. 1.— Emission-line imaging from models A1 (top four panels) and A2 (bottom four panels). For each model, H $\beta$ , [O III] $\lambda$ 5007, He II $\lambda$ 4686, and [N II] $\lambda$ 6583 intensity maps are shown. Both axes are in pixels.
- Fig. 2.— Same as Fig. 1 for models B1 (top four panels) and B2 (bottom four panels). Both axes are in pixels.
- Fig. 3.— [S II] density map (from 200 to 900 cm $^{-3}$ ) for models B1 (top) and B2 (bottom). The axes are in pixels.
- Fig. 4.— Size and positions of the aperture (top) used to obtain the [O III] velocity profiles shown in the bottom nine panels for model A1; The nebula is rotated by 50 $^{\circ}$  around the  $z$  axis and projected on the  $y$  direction. The axes are in pixels. The emission-line profiles (bottom) are normalized.
- Fig. 5.— [O III] line image (top left), P-V diagrams obtained through centered horizontal and vertical slits (top right and bottom left, respectively), and iso-velocity contours for  $V = 9$  km/s.  $z$  and  $y$  are given in pixels.

Model	A1	A2	B1	B2
$T_{eff}$ (K)	150000	150000	90000	90000
$L/L_{\odot}$	9260	9260	150	150
$n_H(\text{cav})$ ( $\text{cm}^{-3}$ )	0	0	400	400
$n_H(\text{shell})$ ( $\text{cm}^{-3}$ )	2000-4000	3000	550 - 1100	825
$R_{inner}/10^{17}\text{cm}$	1.	0.5-1.5	1.	0.5 - 1.5
$H\beta$ ( $10^{35}\text{erg/s}$ )	1.89	1.88	.048	.047
HeII4686	.330	.328	.065	.065
[OI]6300+6363	.227	.232	.402	.392
[OII]3727	1.83	1.97	2.72	2.63
[OIII]5007+4959	24.0	23.6	6.72	6.92
[OIII]4363	.202	.197	.018	.019
[NII]6583+6548	1.88	1.90	3.08	2.99
[NII]5755	.032	.032	.034	.033
[SII]6718	.201	.213	.608	.598
[SII]6732	.297	.307	.624	.607
$T_{[OIII]}$ (K)	12173	12122	8558	8567
$\langle T_e \rangle_{5007}$ (K)	12021	11978	8591	8596
$T_{[NII]}$ (K)	11621	11565	9568	9586
$\langle T_e \rangle_{6583}$ (K)	11194	11225	9582	9612
$n_{[SII]}$ ( $\text{cm}^{-3}$ )	2313	2083	657	629
$\langle n_e \rangle_{6718}$ ( $\text{cm}^{-3}$ )	2491	2272	655	620

Table 1: Input parameters: effective temperature and luminosity of the central ionizing black body, cavity density, shell density, cavity radius or the semi-axis of the elliptical cavity (top). Emission line intensities relative to  $H\beta$  (middle). Physical quantities determined from line ratios and from average calculations, see §2.5 (bottom).

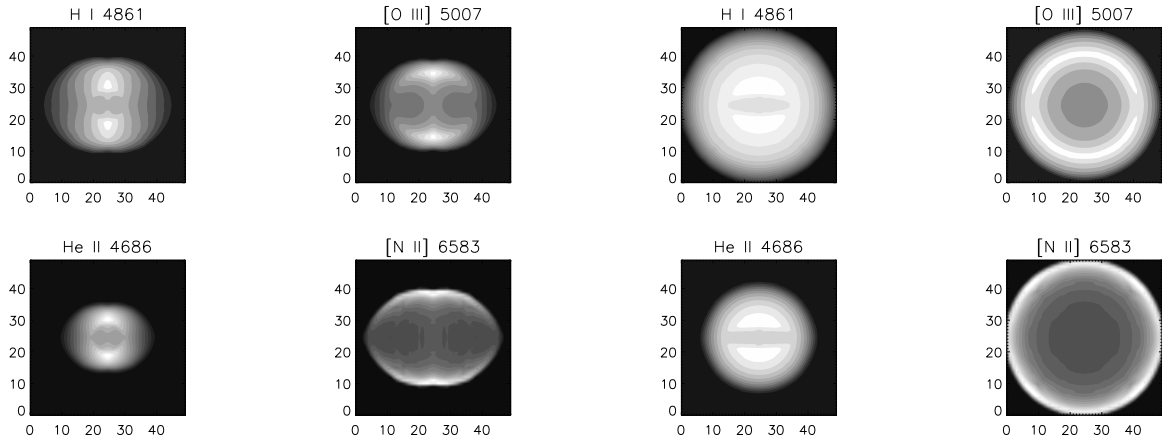


Fig. 1.—

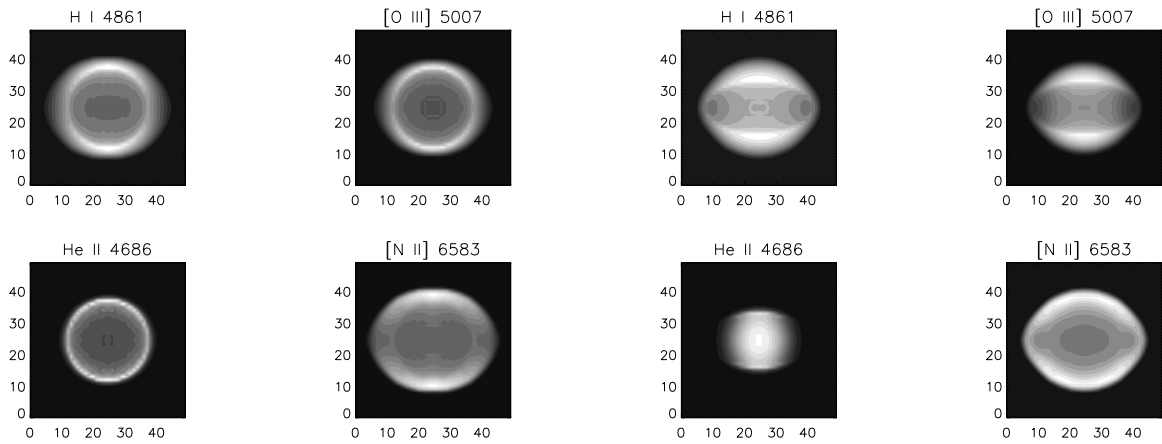


Fig. 2.—

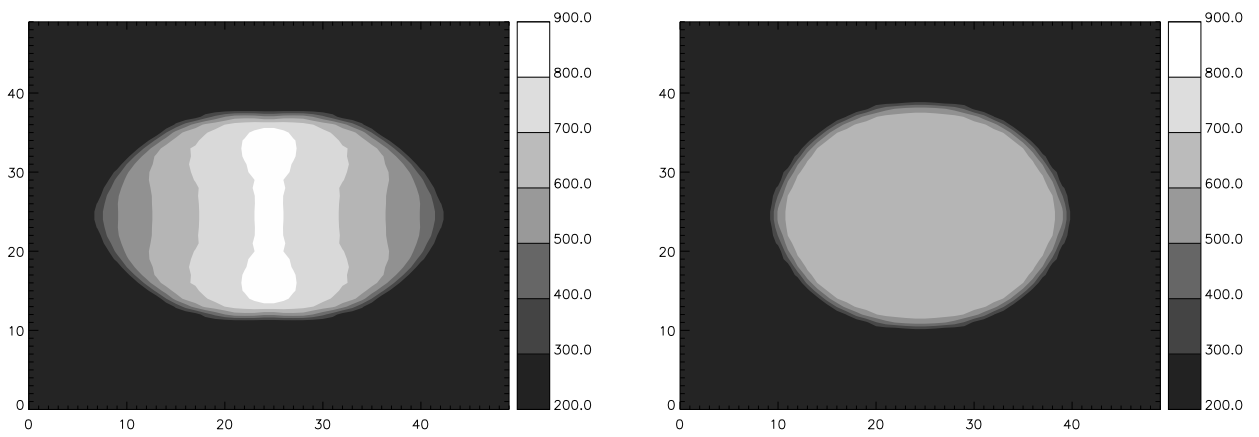


Fig. 3.—

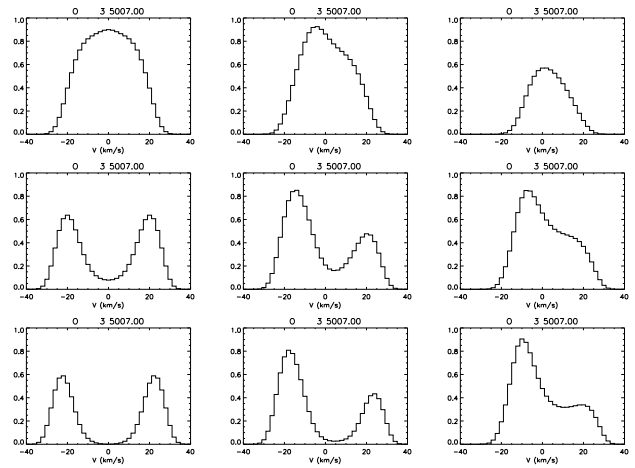
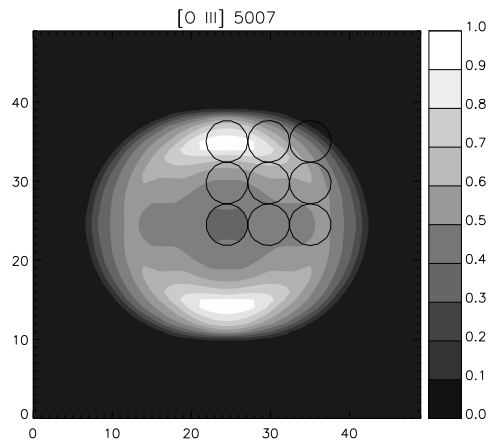


Fig. 4.—

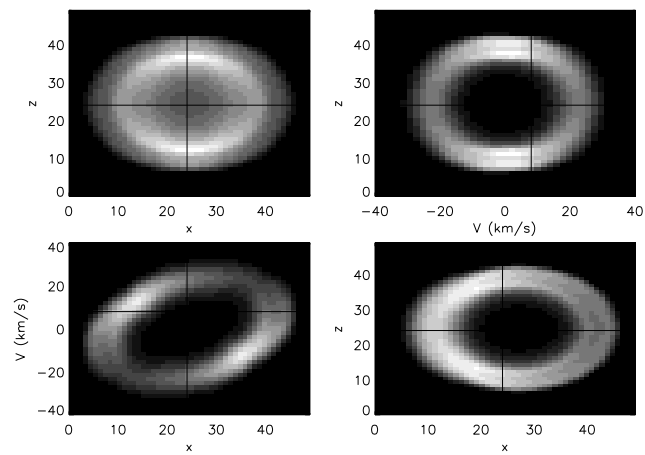


Fig. 5.—